RSC Advances

PAPER

View Article Online
View Journal | View Issue

Cite this: *RSC Adv.*, 2022, **12**, 12355

A reasonably constructed fluorescent chemosensor based on the dicyanoisophorone skeleton for the discriminative sensing of Fe^{3+} and Hg^{2+} as well as imaging in HeLa cells and zebrafish†

Chuqi Zhang, Xinyan Lv, Xiuhong Liu,* Hongyun Chen* and Haifeng He

Received 1st March 2022
Accepted 4th April 2022

DOI: 10.1039/d2ra01357f

rsc.li/rsc-advances

In this study, a new fluorescent sensor dicyanoisophorone Rhodanine-3-acetic acid (DCI-RDA) (DCI-RDA) has been developed by employing a DCI-based push–pull dye as the fluorophore and RDA as the recognition moiety for the simultaneous sensing of Fe^{3+} and Hg^{2+} with a large Stokes Shift (162 nm), high selectivity and sensitivity, and low LOD (1.468 μM for Fe^{3+} and 0.305 μM for Hg^{2+}). In particular, DCI-RDA has a short response time (30 s). The Job's plot method in combination with ^1H NMR titration and theoretical calculations was used to determine the stoichiometry of both DCI-RDA-Fe^{3+}/Hg^{2+} complexes to be 1 : 1. Moreover, DCI-RDA is applied as a fluorescent probe for imaging in HeLa cells and zebrafish, indicating that it can be potentially applied for Fe^{3+}/Hg^{2+} sensing in the field of biology.

1. Introduction

Different elements play different roles in the human body; for example, iron is the most important, abundant, and sophisticated transition metal within these metal cations, which exist in the structure of numerous proteins and enzymes. Normal iron concentration levels are very essential for the human body because it is responsible for a variety of cell functions including electron transfer, transcriptional regulation, and oxygen uptake.[1–3] Insufficient or excess iron can cause numerous diseases such as cancer, Alzheimer's disease, Parkinson's disease, renal injury, and iron deficiency anemia.[4–6] On the other hand, mercury is widely used today; it exists in three forms, namely, elemental, inorganic and organic mercury. Hg^{2+} ions can be converted into methyl mercury, which is one of the most powerful neurotoxins for mammals.[7] Numerous studies have shown that mercury is one of the most toxic heavy metal ions in the living system, and even low doses of mercury may lead to neurological symptoms, damage to the kidneys, brain and hormonal immunological changes because mercury cations can coordinate with sulfur-containing enzymes and proteins.[8] In addition, since the nervous system is highly sensitive to mercury, its exposure may cause hallucinations, impaired consciousness, and other irreversible life-threatening complications.[9] According to the U.S. EPA, the limit value of iron in drinking water is 0.3 mg L^{-1}, while for mercury, the permitted limit is only 0.002 mg L^{-1}.[10] Therefore, it is quite urgent to develop a new, fast, highly sensitive and highly selective method to detect Fe^{3+} and Hg^{2+} in *in vivo* and environment systems.

Nowadays, a variety of traditional analytical methods are widely used for the qualitative and quantitative detection of these two ions, such as atomic absorption spectrometry (AAS),[11] atomic fluorescence spectrometry (AFS),[12] inductively coupled plasma mass spectrometry (ICP-MS),[13] and electrochemical methods.[14] Although the instrument methodology has the advantages of high sensitivity and small injection volume, it is not only inconvenient to maintain the instrument but also needs complex sample pretreatments and professional operators.[15] Thus, researchers have been paying extensive attention to the development of chemosensors to monitor cations due to their relatively low-cost, fast response, and sensitivity for gaining information in real-time even in living cells and organisms.[16–18] To date, a large number of fluorescent chemosensors for the selective and sensitive detection of Hg^{2+},[19–24] and Fe^{3+} (ref. 25–27) have been reported, but most of them can only detect one target. It is well known that bifunctional and multifunctional fluorescent sensors utilize a single host to recognize two or more analytes by distinct fluorescence responses through the same or different channels. Compared with the one-to-one analysis method, the detection of multiple targets with a single sensor is more efficient, hence attracting increasing the attention to this type probe.[28] However, very few sensors have been reported for the simultaneous detection of Hg^{2+} and Fe^{3+}.[29–32] Besides, sensors with a long emission wavelength have deeper tissue penetration and minimal background fluorescence.[33,34] On top of that, fluorescent probes with

School of Chemistry and Chemical Engineering, Jiangxi Science and Technology Normal University, Nanchang 330013, People's Republic of China. E-mail: xiuhong0627@163.com; chenhongyun92@126.com

† Electronic supplementary information (ESI) available. See https://doi.org/10.1039/d2ra01357f

relatively small Stokes shifts restrict their further biodetection, while those with large Stokes shifts can effectually reduce interferences resulting from self-absorption by increasing spectral separation between excitation and emission bands.[35] Therefore, a chemosensor that meets these requirements would be pretty meaningful.

Dicyanoisophorone (DCI) derivatives have shown unique optoelectronic properties and promising applications in fluorescence analyses.[36] They are extremely suitable for developing the aforesaid chemosensor. As fluorophore scaffolds for sensing applications, DCI-based donor–π–acceptor (D–π–A) dyes have some advantageous features including tunable structures, large Stokes shifts, and a long emission wavelength window.[37] The optical properties of DCI-based D–π–A dyes depend on the strength of the donor and acceptor groups.[38] Even more, both S and O on Rhodanine-3-acetic acid (RDA) have lone electron pairs, which are easily contributed to coordinate with metal ions. RDA is chosen as a recognition unit for the detection of metal ions.[39]

Hence, a new dual-functional fluorescent sensor DCI-RDA was constructed for the simultaneous sensing of Fe^{3+} and Hg^{2+} by using a DCI-based push–pull dye as the fluorophore and RDA as the recognition moiety (Fig. 1). The probe showed long wavelength emission, excellent selectivity and sensitivity toward Fe^{3+}/Hg^{2+}. Furthermore, the probe with low cytotoxicity has been successfully applied to fluorescent imaging to detect Fe^{3+}/Hg^{2+} in living cells. The details of the research are carefully discussed below.

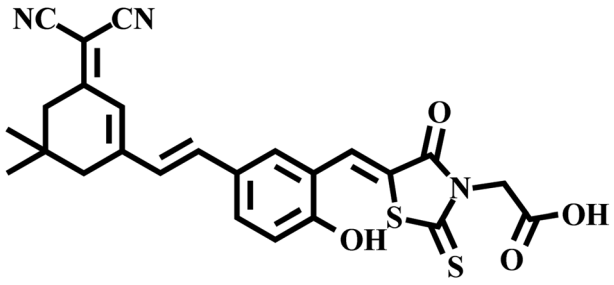

Fig. 1 Molecular structure of probe DCI-RDA.

2. Results and discussion

2.1. Synthesis and characterization

The synthetic pathways are shown in Scheme S1.† Synthetic procedures involving air-sensitive reagents were performed under an argon atmosphere. The intermediate M1, M2 and M3 were synthesized according to a previously reported method.[40] All compounds were purified in the silica column. Characterizations including ^{1}H NMR, ^{13}C NMR, and HRMS spectroscopy techniques were performed to confirm the chemical structure of DCI-RDA. All the protons and carbon atoms (Fig. S1 and S2†) were unambiguously assigned.

2.2. Selectivity and specificity of the sensor DCI-RDA towards Hg^{2+}/Fe^{3+} ions

The fluorescence experiments were first performed to test the selectivity of probe DCI-RDA (20 μM) for Hg^{2+}/Fe^{3+}, with various competitive metal ions including Ni^{2+}, Mn^{2+}, Al^{3+}, Sr^{2+}, Hg^{2+}, Cd^{2+}, Mg^{2+}, Zn^{2+}, Co^{2+}, Cr^{3+}, Pb^{2+}, Fe^{3+}, Ag^{+}, Ca^{2+}, Ba^{2+}, K^{+}, Sn^{2+}, and Cu^{2+} (280 μM) in ethanol solution, respectively. As displayed in Fig. 2a, the addition of Fe^{3+} or Hg^{2+} to the solution of sensor DCI-RDA resulted in a strong fluorescence quenching effect with the excitation wavelength of 460 nm, particularly Fe^{3+}. However, the other metal ions displayed no obvious changes in the fluorescence intensity. The fluorescence photographs shown in Fig. 2b also demonstrated that only Fe^{3+} and Hg^{2+} can cause a significant fluorescence quenching phenomenon. This effect can be ascribed to the formation of a coordinate complex between Fe^{3+}/Hg^{2+} and the O/S atoms of the DCI-RDA sensor, while other metal ions failed to coordinate with the DCI-RDA sensor because of their unsuitable ionic radii, different configurations of extra-nuclear electron and insufficient binding capacity.

In order to examine the specificity of the probe DCI-RDA towards Hg^{2+}/Fe^{3+} ions, competition experiments were conducted with the addition of relevant analytes Ni^{2+}, Mn^{2+}, Al^{3+},

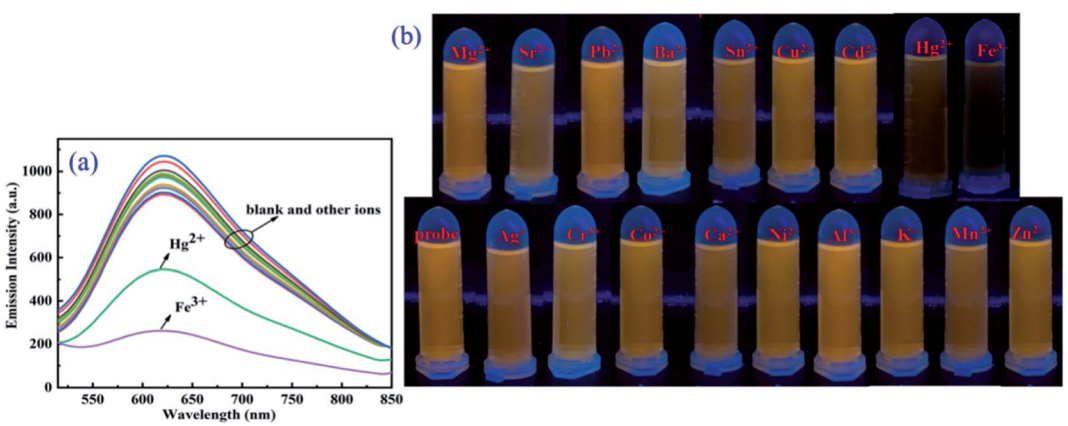

Fig. 2 (a) Fluorescence spectra of probe DCI-RDA (20 μM) with various metal ions (280 μM) in ethanol solution; (b) color changes of the DCI-RDA solution (20 μM) with various metal ions (280 μM) added under a UV-vis lamp (365 nm). EX slit: 5.0 nm, EM slit:10.0 nm, $T = 25$ °C.

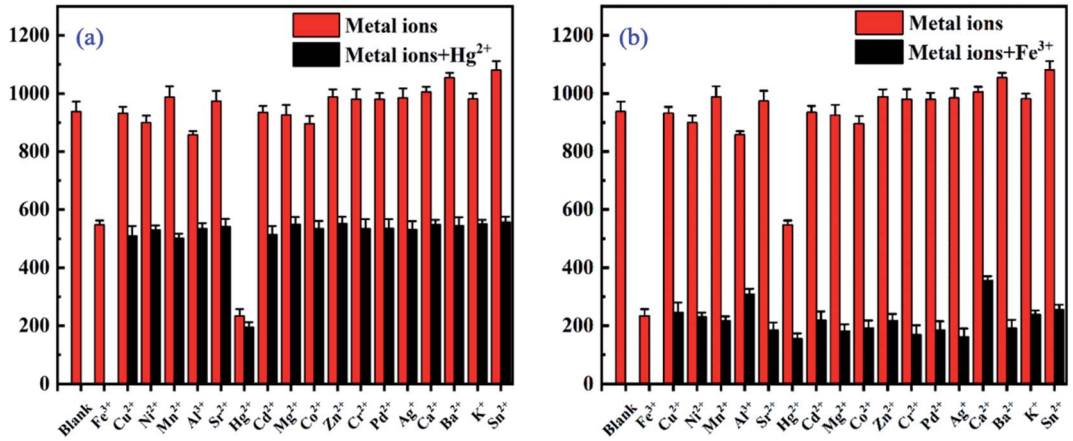

Fig. 3 Fluorescence response of DCI-RDA (20 μM) with Hg^{2+} (22 μM, (a)) and Fe^{3+} (280 μM, (b)) ion in the coexistence of other metal ions (280 μM) in ethanol solution. EX slit: 5.0 nm, EM slit: 10.0 nm, $T = 25$ °C.

Sr^{2+}, Cd^{2+}, Mg^{2+}, Zn^{2+}, Co^{2+}, Cr^{3+}, Pb^{2+}, Ag^{+}, Ca^{2+}, Ba^{2+}, K^{+}, Sn^{2+}, and Cu^{2+} (280 μM) to the probe solution (20 μM) in the presence of Hg^{2+}/Fe^{3+} ions. As depicted in Fig. 3, the fluorescence intensity of the DCI-RDA sensor reduced by 70% after the addition of Fe^{3+} and reduced by 45% after the addition of Hg^{2+}, whereas the competitive metal ions showed almost negligible interference to the fluorescence intensity of DCI-RDA. The above-mentioned results clearly indicated that the presence of competitive metal ions show little effect on the specific detection of Hg^{2+}/Fe^{3+}.

2.3. Determination of Hg^{2+} and Fe^{3+}

In case of the coexistence of Hg^{2+} and Fe^{3+}, the current detection conditions cannot distinguish Fe^{3+} from Hg^{2+}. It is more meaningful to distinguish Fe^{3+} from Hg^{2+} when both of them coexist in the solution. Through a series of experiments, we found that F^{-} can be used to distinguish Fe^{3+} from Hg^{2+}. As shown in Fig. 4a, the fluorescence intensity of the DCI-RDA solution is quenched with the addition of Fe^{3+}, but it would restore close to the original intensity of the free sensor DCI-RDA after the addition of F^{-}. In addition, the addition of F^{-} to the free probe DCI-RDA solutions has no influence on the fluorescence intensity. Nevertheless, there is no change in the fluorescence intensity of DCI-RDA-Hg^{2+} solutions with the addition of F^{-} (Fig. 4b). This is because the added F^{-} reacts with the Fe^{3+} of the Fe^{3+}-DCI-RDA complex and releases the sensor DCI-RDA, which indicates that the binding affinity between Fe^{3+} and F^{-} is more powerful than that of Fe^{3+} and sensor DCI-RDA. However, F^{-} failed to compete with DCI-RDA for Hg^{2+} because F^{-} is not a good chelating ligand of Hg^{2+}. Therefore, the sensor can be used for the separate detection of Hg^{2+} and Fe^{3+} with the addition of F^{-} when Hg^{2+} and Fe^{3+} coexist in the sample.

2.4. Sensitivity of the sensor DCI-RDA towards Hg^{2+}/Fe^{3+} ions

To demonstrate the sensitivity of the sensor DCI-RDA towards Hg^{2+} and Fe^{3+} ions, fluorescence titration experiments were carried out with various concentrations of Fe^{3+} and Hg^{2+} in ethanol solution. As shown in Fig. 5, the fluorescence titration was carried out with Hg^{2+} (0–1.1 equiv.) and Fe^{3+} (0–14 equiv.)

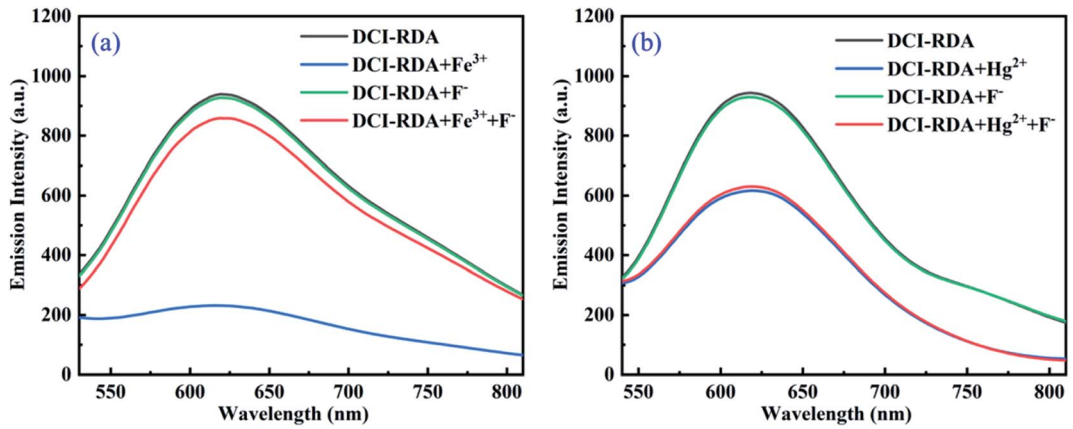

Fig. 4 Fluorescence emission spectra of the DCI-RDA solution with different additives (a) 280 μM Fe^{3+}, 340 μM F^{-}; (b) 22 μM Hg^{2+}, 66 μM F^{-} in ethanol solution, respectively. EX slit: 5.0 nm EM slit: 10.0 nm, $T = 25$ °C.

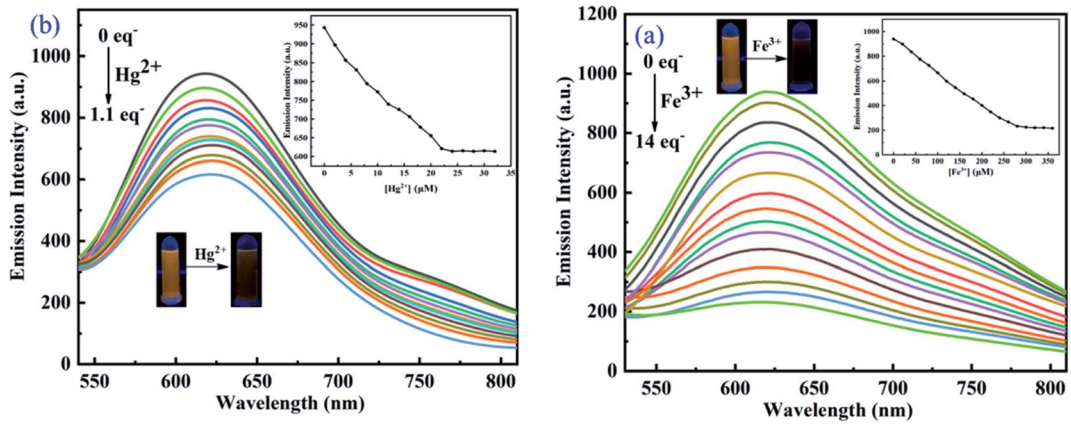

Fig. 5 (a) Fluorescent spectroscopic of DCI-RDA titrated with 0–22 μM of Hg^{2+} in ethanol solution; (b) fluorescent spectra of DCI-RDA titrated with 0–280 μM of Fe^{3+} solutions with $\lambda_{ex} = 460$ nm, $\lambda_{em} = 622$ nm in ethanol solution. EX slit: 5.0 nm EM slit: 10.0 nm, $T = 25$ °C.

addition and showed a subsequent gradual weakening in the fluorescence intensity with the increase in the ion concentration. Hg^{2+} and Fe^{3+} could lead to the stable weakening of the fluorescence intensity, and a plateau was formed upon the addition of 22 μM and 280 μM, respectively. It is also observed that the fluorescence color changed from yellow to faint yellow (Fig. 5a inset). The above-mentioned phenomenon showed that the probe DCI-RDA provided a fluorescence quenched behavior for the selective detection of Hg^{2+} and Fe^{3+}. Importantly, a linear relationship between fluorescence intensity and Hg^{2+} concentrations is obtained with $R^2 = 0.992$ in the range of 0–22 μM (Fig. S3A†). The limit of detection (LOD) of the sensor DCI-RDA was calculated to be 0.305 μM for Hg^{2+} from the respective calibration curve based on the formula shown in Calculation S3.1 (see ESI S3.1†). Also, there is a linear relationship between the fluorescence intensity and Fe^{3+} concentrations from 0 to 225 μM with $R^2 = 0.998$ (Fig. S3B†). The LOD of Fe^{3+} was calculated to be 1.468 μM, which is lower than the limit of Fe^{3+} in drinking water (5.357 μM) set by U.S. Environmental Protection Agency.[10] These results indicate that the fluorescent probe has potential application in the detection of Hg^{2+} and Fe^{3+}. On the other hand, the binding constant of the DCI-RDA sensor with Hg^{2+} and Fe^{3+} were determined to be 4.095×10^4 M^{-1} and 3.297×10^3 M^{-1}, respectively, from the corresponding slope of the linear (Fig. S4†) following the formula shown in S3.2 (see ESI S3.2†).

The advantage of quick response of the probe is very important for practical applications. Therefore, the response time of DCI-RDA to Fe^{3+} and Hg^{2+} was also detected. At first, the fluorescence intensity of DCI-RDA (20 μM) was extremely strong and constant. However, after adding Fe^{3+} (280 μM) or Hg^{2+} (22 μM) in the DCI-RDA solution, DCI-RDA could quickly respond to Fe^{3+}/Hg^{2+}. The fluorescence intensity decreased dramatically and reached fluorescence quenching within 30 s (Fig. S5†), which means that the probe can be used for real-time detection.

2.5. The binding analysis

To better understand the binding process, the stoichiometry of the DCI-RDA sensor and Hg^{2+}/Fe^{3+} was investigated by the Job's plot analysis based on the fluorescence test (Fig. S6†). From the results, we can clearly see a turning point at 0.5 M fraction of Hg^{2+}/Fe^{3+} ions, indicating a stoichiometric ratio of 1 : 1 for both DCI-RDA-Hg^{2+} and DCI-RDA-Fe^{3+} complexes. Thus, it is predicted that there was only one binding site in the DCI-RD sensor A for both Hg^{2+} and Fe^{3+}.

In addition, ^{1}H NMR titration experiments were carried out in DMSO-d_6 to clarify the binding interactions between the DCI-RDA sensor and Hg^{2+}. As shown in Fig. 6, DCI-RDA shows two characteristic peaks at δ 4.74 ppm (H_a) and δ 7.98 ppm (H_b), which are assigned to the methylene proton of acetic acid and attached to C=C, respectively. The proton signals of H_a and H_b had a more apparent change with the new peak appearing at δ 4.38 ppm and δ 8.10 ppm, and became gradually intensified with 0.3 equiv. Hg^{2+} addition due to their location in the vicinity of the Hg^{2+} binding site. On the other hand, the proton signals of H_c, which is assigned to the carboxyl proton of acetic acid slowly weakened and disappeared with 0.3 equiv. Hg^{2+} addition. Nevertheless, the proton signals of H_d, which is assigned to Ph-OH, showed no change, except the change in the peak shape (Table S1†). These results indicated that S^1 and O^1 acted as electron donors for coordination to Hg^{2+}. Unfortunately, it is difficult to carry out the ^{1}H NMR titration experiments for DCI-RDA toward Fe^{3+} due to the paramagnetic property of Fe^{3+}.

2.6. Theoretic calculations

To further demonstrate the sensing mechanism of the DCI-RDA sensor toward Hg^{2+} and Fe^{3+} ions, density functional theory (DFT) calculations were carried out to provide reasonable theoretical explanations on the coordinate interaction. All calculations were carried out using the Gaussian 09 software.[41] The geometry of all studied structures were calculated in the gas phase by using the wB97XD level since this function contains the dispersion interaction term and is more appropriate for calculating the optimized structures of compounds and the non-covalent interactions between compounds,[42] together with vibrational frequency calculation at the same level of theory to ensure that all optimized structures are true energy minima without imaginary frequency. The C, H, O and N atoms were

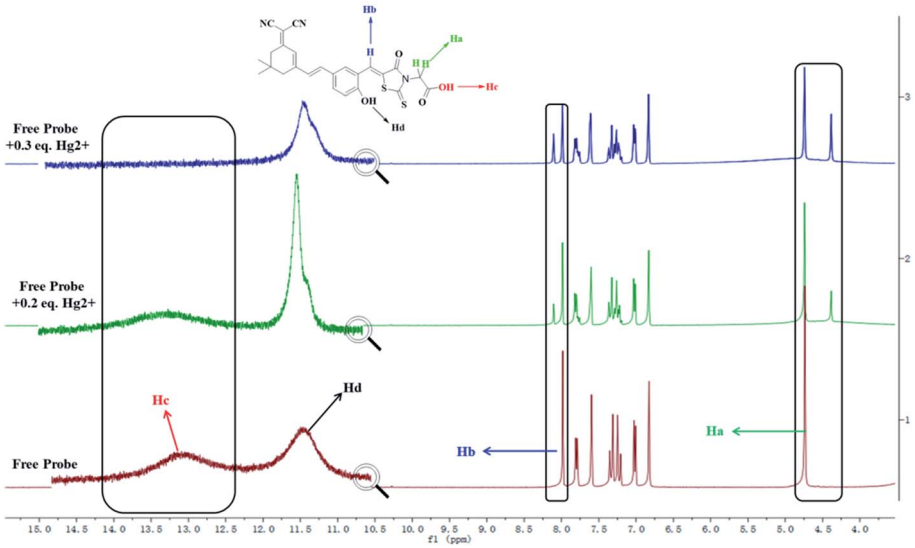

Fig. 6 ^{1}H NMR titration spectra of DCI-RDA with Hg^{2+} ions in DMSO-d_6.

described by the 6-31G(d,p) basis set, and the LANL2DZ[43,44] was employed for the Fe and Hg atoms with effective core potentials (ECPs) for its core electrons. As shown in Fig. 7, the molecular structure of the DCI-RDA sensor suffers changes after interacting with $Hg^{2+}$and Fe^{3+}. The oxygen atom (O^1) of COOH and sulfur atom (S^1) of C=S in the DCI-RDA sensor coordinated with Hg^{2+}/Fe^{3+} ions to form DCI-RDA-Hg^{2+} and DCI-RDA-Fe^{3+} complexes. The complexes revealed a 1 : 1 stoichiometric ratio for the sensor and Hg^{2+}/Fe^{3+}, which is in conformity with the results obtained from the Job's plots analysis and ^{1}H NMR titration experiments. From the geometry of the sensor DCI-RDA-Hg^{2+} complex, we can clearly see the bond length of Hg–O^1 and Hg–S^1 is 2.1424 Å and 2.5516 Å, respectively, indicating that the coordination between Hg^{2+} and O^1 atom is stronger. Similar results can be obtained in the DCI-RDA-Fe^{3+} complex. Compared with the DCI-RDA-Hg^{2+} complex, the interaction between Fe^{3+} and the sensor is stronger due to the shorter bond length of Fe–O^1 and Fe–S^1.

The orbital energy levels of probe DCI-RDA and DCI-RDA-Fe^{3+}/Hg^{2+}, including LUMO and HOMO energy levels, are shown in Fig. S7.† On the LUMO and HOMO of the DCI-RDA probe, the electron density was mainly distributed on the DCI and benzene ring part. However, after Hg^{2+} coordinated with the O^1 atom and S^1 atom of DCI-RDA, on the HOMO of DCI-RDA-Hg^{2+} complex, the electron density was still focused on the DCI and benzene ring part, while the distribution of LUMO in the DCI-RDA-Hg^{2+} complex was changed to the RDA moiety. Completely opposing results were obtained in the DCI-RDA-Fe^{3+} complex, that is, the HOMO of the DCI-RDA-Fe^{3+} complex was focused on the RDA moiety, while the distribution of LUMO was changed to the DCI

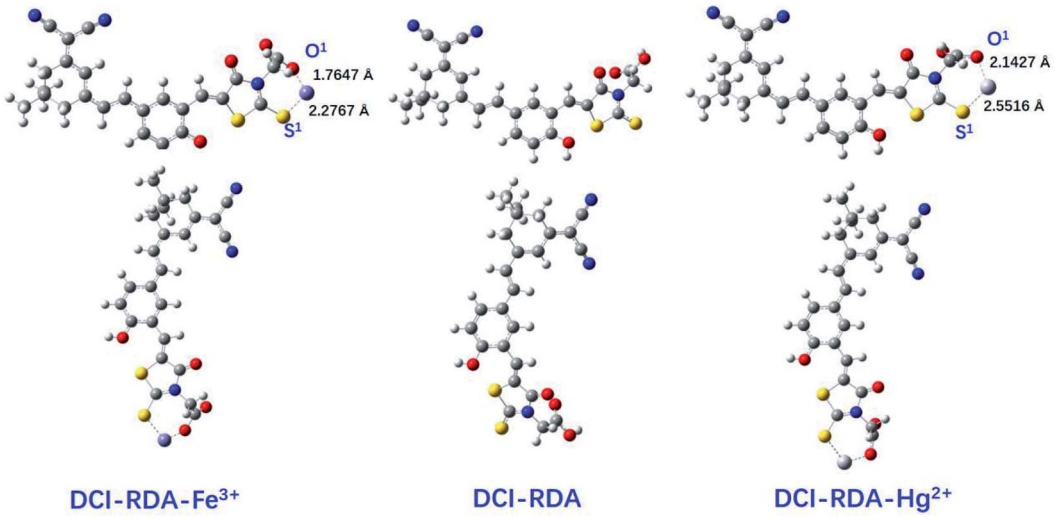

Fig. 7 The optimized geometric structures based on wB97XD and PCM salvation model for DCI-RDA and DCI-RDA-Hg^{2+}/Fe^{3+} in the gas phase. Here, both top views and side views are shown.

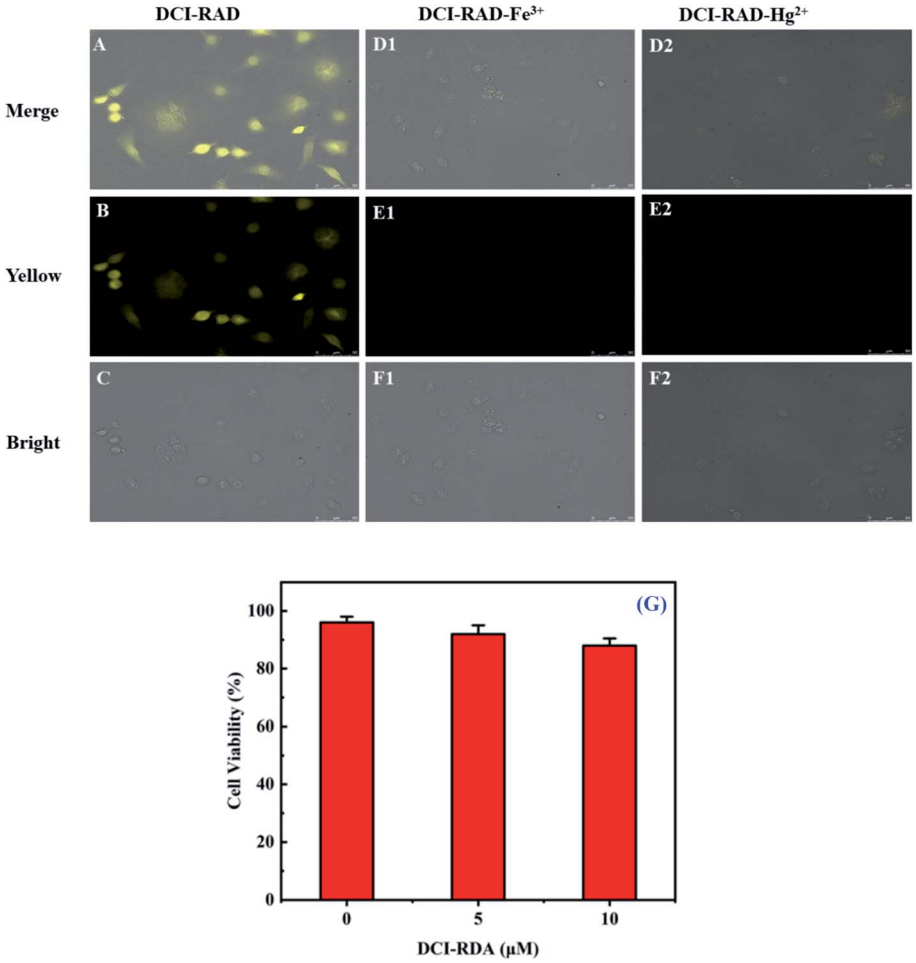

Fig. 8 Fluorescence imaging of HeLa cells incubated with DCI-RDA (10 μM) for 30 min (A–C), and then with Hg^{2+}/Fe^{3+} (100 μM) for another 30 min (D–F). The cytotoxicity of DCI-RDA against HeLa cells incubated with different concentrations of DCI-RDA for 24 h (G).

and benzene ring part. The above phenomenon indicated a clear ICT in both DCI-RDA-Hg^{2+} and DCI-RDA-Fe^{3+} complexes.

Furthermore, the HOMO and LUMO energy gap of DCI-RDA was calculated to be 6.65 eV, while it was 5.61 eV for DCI-RDA-Hg^{2+} and 3.79 eV for DCI-RDA-Fe^{3+}. After the combination of DCI-RDA and Hg^{2+}/Fe^{3+}, the HOMO and LUMO bandgaps were reduced from 6.65 to 5.61 eV and 3.79 eV, respectively. The decrease in the calculated energy gap between HOMO and LUMO, after DCI-RDA adducting with Hg^{2+}/Fe^{3+}, indicated the strong binding of Hg^{2+}/Fe^{3+} to the probe. These calculated results further support our experimental observation based on spectrophotometric experiments.

2.7. Fluorescence imaging for living cells and zebrafish

Herein, the practical application of the DCI-RDA sensor for the determination of Hg^{2+}/Fe^{3+} in biological media in living cells was investigated using human HeLa cells. First, the cell cytotoxicity of the DCI-RDA sensor against HeLa cells was studied by the MTT assay.[45] The result revealed that the free sensor DCI-RDA has negligible toxicity on HeLa cells and more than 88% survival after 24 h (Fig. 8G), indicating that the DCI-RDA sensor has low cytotoxicity and great biocompatibility in biological systems.

Furthermore, the cell imaging of the DCI-RDA sensor in HeLa cells was studied (Fig. 8), a bright fluorescence signal (Fig. 8B) was observed after the incubation of HeLa cells with the DCI-RDA sensor (10 μM) for 30 min. Due to the large Stokes shift (162 nm) of the DCI-RDA sensor, it can effectually reduce interferences resulting from self-absorption. Amazingly, very low dim fluorescence (Fig. 8E1 and E2) in the intracellular region can be observed, followed by the treatment with Hg^{2+}/Fe^{3+} (100 μM) incubating for another 30 min. This phenomenon confirmed that the probe DCI-RDA could penetrate into the cells and can be used to track Hg^{2+}/Fe^{3+} in living cells by fluorescent imaging.

To demonstrate the further applications of probe DCI-RDA in living organisms, fluorescence imaging was carried out in zebrafish, which have optical transparency and similar genetic properties to humans. As shown in Fig. 9, when the zebrafish was cultivated with DCI-RDA for 1 h, the strong yellow fluorescence in the digestive system of the zebrafish larvae is clearly visible (Fig. 9A). However, in the presence of Hg^{2+}, yellow fluorescent evidently weakened (Fig. 9B) after washing three times

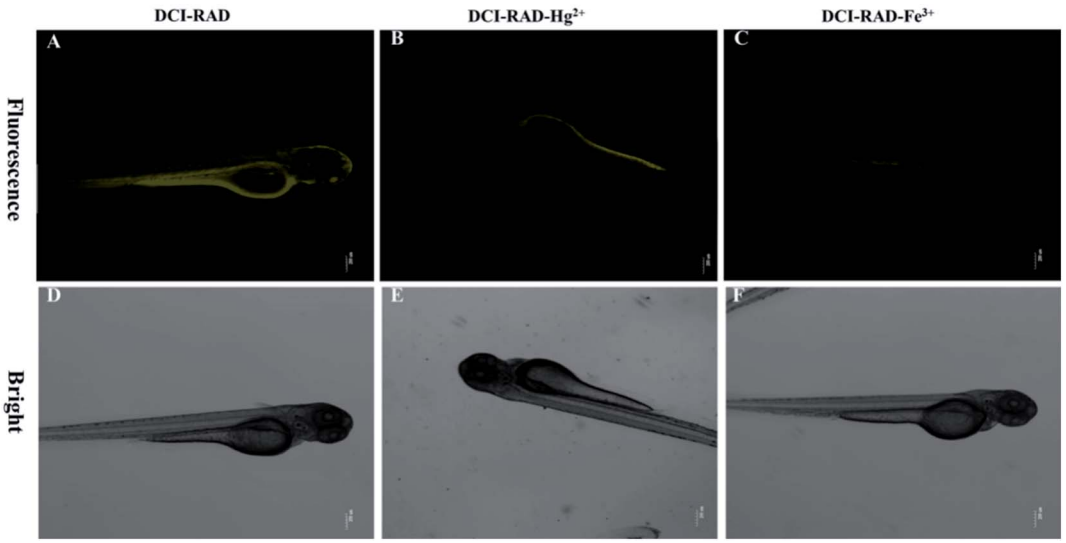

Fig. 9 Fluorescence imaging of zebrafish larvae treated with DCI-RDA (10 μM) for 1 h (A), and further treated with Hg^{2+} (100 μM, (B)) or Fe^{3+} (100 μM, (C)) for another 1 h, (D–F) is the bright field picture of (A–C), respectively.

in the surface of zebrafish with PBS buffer. Nevertheless, in the presence of Fe^{3+}, the yellow fluorescent basically disappeared (Fig. 9C). These results clearly indicate that DCI-RDA is organism-permeable and is significantly sensitive for detecting Hg^{2+} and Fe^{3+} in the living body.

3. Conclusions

In summary, a new dual-functional fluorescent sensor DCI-RDA was constructed for the simultaneous sensing of Fe^{3+} and Hg^{2+}, by using a DCI-based push–pull dye as the fluorophore and RDA as the recognition moiety. The favorable attributes of the probe DCI-RDA include a remarkably large Stokes shift (162 nm), rapid response, high selectivity and sensitivity, and effective detection of Hg^{2+}/Fe^{3+}. The detection limits for Fe^{3+} and Hg^{2+} ions were 1.468 μM and 0.305 μM, respectively. The LOD of Fe^{3+} is lower than the limit of Fe^{3+} in drinking water (5.357 μM) set by U.S. Environmental Protection Agency, and the LOD of Hg^{2+} is lower compared with the reported work (Table S2†). Furthermore, the stoichiometry of the complexes between DCI-RDA and Hg^{2+}/Fe^{3+} was determined by the Job's method and ^1H NMR titration experiments and found to have a 1 : 1 ratio. DFT studies were carried out to verify the experimental data. Importantly, DCI-RDA exhibited low cytotoxicity against HeLa cells by the MTT assay. The fluorescence imaging in HeLa cells and zebrafish showed that DCI-RDA could be used as an efficient intracellular probe for the detection of Fe^{3+} and Hg^{2+}. These results indicated that DCI-RDA can be utilized as a selective, sensitive and safe probe for the sensing of Fe^{3+} and Hg^{2+} ions in living systems.

Conflicts of interest

There are no conflicts to declare.

Acknowledgements

This work was financially supported by the National Natural Science Foundation of China (21867011); Doctor start foundation project of Jiangxi Normal University of Science and Technology (2019BSQD003); The Jiangxi Normal University of Science and Technology youth talent program (2020QNBJRC003); Innovation and entrepreneurship of college students (202011318014).

Notes and references

1 S. O. Tümay, *J. Lumin.*, 2021, **231**, 117813.
2 X. Y. Meng, L. You, S. Y. Li, Q. Sun, X. G. Luo, H. F. He, J. L. Wang and F. Zhao, *RSC Adv.*, 2020, **10**, 37735.
3 S. O. Tümay, M. H. Irani-Nezhad and A. Khataee, *Spectrochim. Acta, Part A*, 2021, **248**, 119250.
4 A. Uslu, E. Özcan, S. O. Tümay, H. H. Kazan and S. Yeşilot, *J. Photochem. Photobiol., A*, 2020, **392**, 112411.
5 L. Wang, Y. Q. Fan, X. W. Guan, W. J. Qu, Q. Lin, H. Yao, T. B. Wei and Y. M. Zhang, *Tetrahedron*, 2018, **74**, 4005–4012.
6 Y. Li, H. T. Zhou, W. Chen, G. C. Sun, L. Sun and J. H. Su, *Tetrahedron*, 2016, **72**, 5620–5625.
7 S. O. Tumay, V. Sanko, A. Senocak and E. Demirbas, *New J. Chem.*, 2021, **45**, 14495.
8 W. Y. Lin, X. W. Cao, Y. D. Ding, L. Yuan and L. L. Long, *Chem. Commun.*, 2010, **46**, 3529–3531.
9 H. Y. Qi, X. N. Sun, T. Jing, J. L. Li and J. Li, *RSC Adv.*, 2022, **12**, 1989.
10 S. O. Tümay, M. H. Irani-nezhad and A. Khataee, *Spectrochim. Acta, Part A*, 2021, **261**, 120017.
11 J. Y. Cabon, P. Giamarchi and A. Le Bihan, *Anal. Chim. Acta*, 2010, **664**, 114–120.
12 Y. Liu, J. Zou, B. Luo, H. Yu, Z. Zhao and H. Xia, *Microchem. J.*, 2021, **169**, 106547.

13 E. Bakkaus, R. N. Collins, J. L. Morel and B. Gouget, *J. Chromatogr. A*, 2006, **1129**, 208–215.
14 P. Ugo, L. Moretto, A. De Boni, P. Scopece and G. Mazzocchin, *Anal. Chim. Acta*, 2002, **474**, 147–160.
15 X. Bao, Q. Cao, X. Wu, H. Shu, B. Zhou, Y. Geng and J. Zhu, *Tetrahedron Lett.*, 2016, **57**, 942–948.
16 L. Zhang, Z. Tang, L. Hou, Y. Qu, Y. Deng, C. Zhang, C. Xie and Z. Wu, *Analyst*, 2020, **145**, 1641–1645.
17 M. Zhu, Z. Zhao, X. Liu, P. Chen, F. Fan, X. Wu, R. Hua and Y. Wang, *J. Hazard. Mater.*, 2021, **406**, 124767.
18 Y. Zhu, Q. Sun, J. Shi, H. Xia, J. Wang, H. Chen, H. He, L. Shen, F. Zhao and J. Zhong, *J. Photochem. Photobiol., A*, 2020, **389**, 112244.
19 M. Saleem and K. H. Lee, *RSC Adv.*, 2015, **5**, 72150.
20 M. C. Ríos, N. F. Bravo, C. C. Sanchez and J. Portilla, *RSC Adv.*, 2021, **11**, 34206.
21 Z. Q. Yan, M. F. Yuen, L. Hu, P. Sun and C. S. Lee, *RSC Adv.*, 2014, **4**, 48373–48388.
22 C. T. Shi, Z. Y. Huang, A. B. Wu, Y. X. Hu, N. C. Wang, Y. Zhang, W. M. Shu and W. C. Yu, *RSC Adv.*, 2021, **11**, 29632–29660.
23 L. Huang, W. L. Sheng, L. Z. Wang, X. Meng, H. D. Duan and L. Q. Chi, *RSC Adv.*, 2021, **11**, 23597.
24 W. Yao, Y. C. Hua, Z. H. Yan, C. X. Wu, F. Y. Zhou and Y. Liu, *RSC Adv.*, 2021, **11**, 36310.
25 Z. Y. Yin, J. H. Hu, K. Gui, Q. Q. Fu, Y. Yao, F. L. Zhou, L. L. Ma and Z. P. Zhang, *J. Photochem. Photobiol., A*, 2020, **396**, 112542.
26 Z. G. Gao, C. Kan, H. B. Liu, J. Zhu and X. F. Bao, *Tetrahedron*, 2019, **75**, 1223–1230.
27 S. Erdemir, O. Alici, D. Aydin and O. Kocyigit, *J. Mol. Liq.*, 2021, **337**, 116471.
28 B. X. Shen and Y. Qian, *Sens. Actuators, B*, 2018, **260**, 666–675.
29 A. L. Li, Z. L. Wang, W. Y. Wang, Q. S. Liu, Y. Sun, S. F. Wang and W. Gu, *Microchem. J.*, 2021, **160**, 105682.
30 Z. E. Chen, X. F. Zang and H. Zhang, *Spectrochim. Acta, Part A*, 2021, **260**, 119955.
31 T. Savran, S. N. K. Elmas, D. A. S. Arslan, F. N. Arslan and I. Yilmaz, *Res. Chem. Intermed.*, 2022, **48**, 1003.
32 S. N. K. Elmas, Z. E. Dincer, A. S. Erturk, A. Bostanci, A. Karagoz, M. Koca, G. Sadi and I. Yilmaz, *Spectrochim. Acta, Part A*, 2020, **224**, 117402.
33 S. Chen, P. Hou, B. Zhou, X. Song, J. Wu, H. Zhang and J. W. Foley, *RSC Adv.*, 2013, **3**, 11543–11546.
34 L. Yuan, W. Lin, K. Zheng, L. He and W. Huang, *Chem. Soc. Rev.*, 2013, **42**, 622–661.
35 X. Wei, M. Hao, X. X. Hu, Z. Song, Y. Wang, R. Sun, J. Zhang, M. Yan, B. Ding and J. Yu, *Sens. Actuators, B*, 2021, **326**, 128849.
36 Z. Gao, X. Zhang, M. Zheng and Y. Chen, *Dyes Pigm.*, 2015, **120**, 37–43.
37 Y. Zhang, Y. Hao, X. Ma, S. Chen and M. Xu, *Environ. Pollut.*, 2020, **265**, 114958.
38 M. M. Jadhav, D. Patil and N. Sekar, *J. Photochem. Photobiol., A*, 2018, **363**, 13–22.
39 X. Meng, J. Wang, X. Li, Q. Sun, Q. Tu, X. Liu, H. He and F. Zhao, *Microchem. J.*, 2021, **169**, 106551.
40 M. Qian, L. Zhang, Z. Pu, J. Xia, L. Chen, Y. Xia, H. Cui, J. Wang and X. Peng, *J. Mater. Chem. B.*, 2018, **6**, 7916–7925.
41 M. J. Frisch, G. W. Trucks, H. B. Schlegel, G. E. Scuseria, M. A. Robb, J. R. Cheeseman, *et al.*, *Gaussian 09, revision A. 01*, Gaussian, Inc., Wallingford, CT, 2009.
42 **https://gaussian.com/dft/**.
43 W. R. Wadt and P. J. Hay, *J. Chem. Phys.*, 1985, **82**, 284–298.
44 T. Dunning Jr, P. Hay, P. J. Hay and W. R. Wadt, *J. Chem. Phys.*, 1985, **82**, 299–310.
45 C. Huang, J. Qu, J. Qi, M. Yan and G. Xu, *Org. Lett.*, 2011, **13**, 1462–1465.